6
Historical track detectors

A man should look for what is, and not for what he thinks should be.
Albert Einstein

In this chapter some historical particle detectors will be briefly described. These are mainly optical devices that have been used in the early days of cosmic rays and particle physics. Even though some of these detectors have been 'recycled' for recent elementary particle physics experiments, like nuclear emulsions for the discovery of the tau neutrino (ν_τ) or bubble chambers with holographic readout for the measurement of short-lived hadrons, these optical devices are nowadays mainly integrated into demonstration experiments in exhibitions or employed as eye-catchers in lobbies of physics institutes (like spark chambers or diffusion cloud chambers).

6.1 Cloud chambers

The *cloud chamber* ('Wilson chamber') is one of the oldest detectors for track and ionisation measurement [1–4]. In 1932 Anderson discovered the positron in cosmic rays by operating a cloud chamber in a strong magnetic field (2.5 T). Five years later Anderson, together with Neddermeyer, discovered the muon again in a cosmic-ray experiment with cloud chambers.

A cloud chamber is a container filled with a gas–vapour mixture (e.g. air–water vapour, argon–alcohol) at the vapour saturation pressure. If a charged particle traverses the cloud chamber, it produces an ionisation trail. The lifetime of positive ions produced in the ionisation process in the chamber gas is relatively long ($\approx$ ms). Therefore, after the passage of the

https://doi.org/10.1017/9781009401531.009 Published online by Cambridge University Press

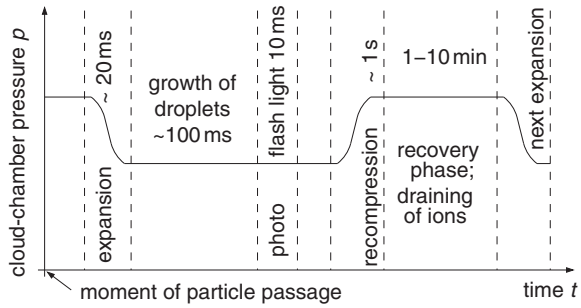

Fig. 6.1. Expansion cycle in a cloud chamber [5].

particle a trigger signal, for example, can be derived from a coincidence of scintillation counters, which initiates a fast expansion of the chamber. By means of adiabatic expansion the temperature of the gas mixture is lowered and the vapour gets supersaturated. It condenses on seeds, which are represented by the positive ions yielding droplets marking the particle trajectory. The track consisting of droplets is illuminated and photographed. A complete expansion cycle in a cloud chamber is shown in Fig. 6.1 [5].

The characteristic times, which determine the length of a cycle, are the lifetime of condensation nuclei produced by the ionisation (≈ 10 ms), the time required for the droplets to grow to a size where they can be photographed (≈ 100 ms), and the time which has to pass after the recording of an event until the chamber is recycled to be ready for the next event. The latter time can be very long since the sensitive volume of the chamber must be cleared of the slowly moving positive ions. In addition, the cloud chamber must be transformed into the initial state by recompression of the gas–vapour mixture.

In total, cycle times from 1 min up to 10 min can occur, limiting the application of this chamber type to rare events in the field of cosmic rays.

Figure 6.2 shows electron cascades initiated by cosmic-ray muons in a multiplate cloud chamber [6, 7].

A *multiplate cloud chamber* is essentially a sampling calorimeter with photographic readout (see Chap. 8 on 'Calorimetry'). The introduction of lead plates into a cloud chamber, which in this case was used in an extensive-air-shower experiment, serves the purpose of obtaining an electron/hadron/muon separation by means of the different interaction behaviour of these elementary particles.

In contrast to the *expansion cloud chamber*, a diffusion cloud chamber is permanently sensitive. Figure 6.3 shows schematically the construction of a *diffusion cloud chamber* [5, 8–11]. The chamber is, like the expansion cloud chamber, filled with a gas–vapour mixture. A constant temperature

https://doi.org/10.1017/9781009401531.009 Published online by Cambridge University Press

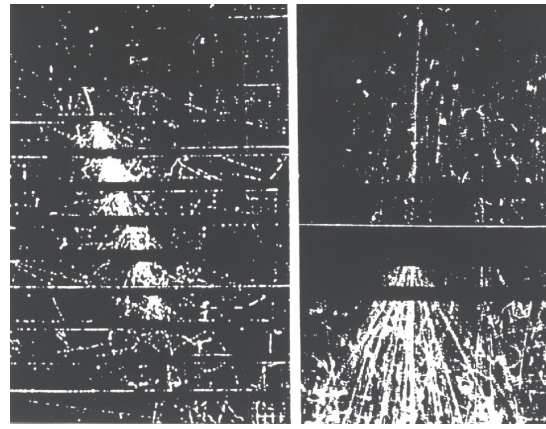

Fig. 6.2. Electromagnetic cascades in the core of an extensive air shower initiated by cosmic-ray muons (presumably via muon bremsstrahlung) in a multiplate cloud chamber [6, 7].

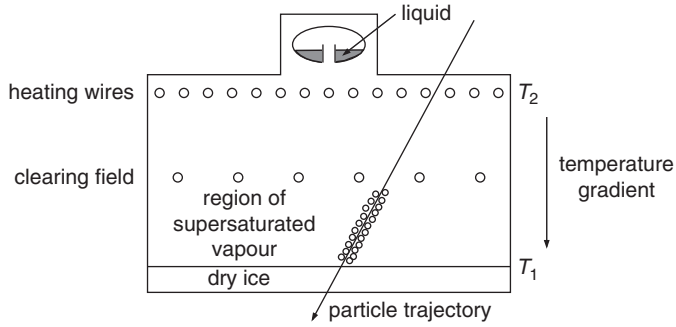

Fig. 6.3. Schematic representation of the construction of a diffusion cloud chamber [5].

gradient provides a region where the vapour is in a permanently supersaturated state. Charged particles entering this region produce a trail automatically without any additional trigger requirement. Zone widths (i.e. regions in which trails can form) with supersaturated vapour of 5 cm to 10 cm can be obtained. A clearing field removes the positive ions from the chamber.

The advantage of permanent sensitivity is obtained at the expense of small sensitive volumes. Since the chamber cannot be triggered, all events, even background events without interest, are recorded.

Because of the long repetition time for triggered cloud chambers and the disadvantage of photographic recording, this detector type is rarely used nowadays.

https://doi.org/10.1017/9781009401531.009 Published online by Cambridge University Press

6.2 Bubble chambers

Bubble chambers [12–17], like cloud chambers, belong to the class of visual detectors and, therefore, require optical recording of events. This method of observation includes the tedious analysis of bubble-chamber pictures which certainly limits the possible statistics of experiments. However, the bubble chamber allows the recording and reconstruction of events of high complexity with high spatial resolution. Therefore, it is perfectly suited to study rare events (e.g. neutrino interactions); still, the bubble chamber has now been superseded by detectors with a purely electronic readout.

In a bubble chamber the liquid (H_2, D_2, Ne, C_3H_8, Freon, etc.) is held in a pressure container close to the boiling point. Before the expected event the chamber volume is expanded by retracting a piston. The expansion of the chamber leads to a reduction in pressure thereby exceeding the boiling temperature of the bubble-chamber liquid. If in this *superheated liquid state* a charged particle enters the chamber, bubble formation sets in along the particle track.

The positive ions produced by the incident particles act as nuclei for bubble formation. The lifetime of these nuclei is only 10^{-11} s to 10^{-10} s. This is too short to trigger the expansion of the chamber by the incoming particles. For this reason the superheated state has to be reached *before* the arrival time of the particles. Bubble chambers, however, can be used at accelerators where the arrival time of particles in the detector is known and, therefore, the chamber can be expanded in time (*synchronisation*).

In the superheated state the bubbles grow until the growth is stopped by a termination of the expansion. At this moment the bubbles are illuminated by light flashes and photographed. Figure 6.4 shows the principle of operation of a bubble chamber [5, 8]. The inner walls of the container have to be extremely smooth so that the liquid 'boils' only in those places where bubble formation should occur, namely, along the particle trajectory, and not on the chamber walls.

Depending on the size of the chamber repetition times down to 100 ms can be obtained with bubble chambers.

The bubble-chamber pressure before expansion is several atmospheres. To transform the gases into the liquid state they generally must be strongly cooled. Because of the large amount of stored gases, the experiments with hydrogen bubble chambers can be potentially dangerous because of the possible formation of explosive oxyhydrogen gas, if the chamber gas leaks from the bubble chamber. Also operation with organic liquids, which must be heated for the operation, represents a risk because of their flammability. Bubble chambers are usually operated in a high magnetic field (several Tesla). This allows to measure particle momenta

https://doi.org/10.1017/9781009401531.009 Published online by Cambridge University Press

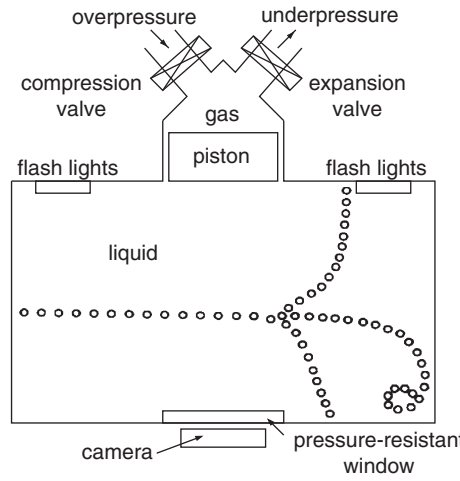

Fig. 6.4. Schematic construction of a bubble chamber [5, 8].

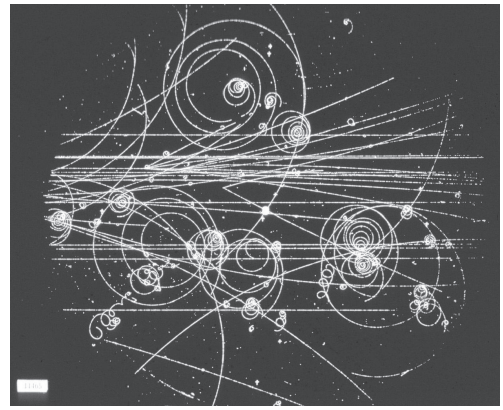

Fig. 6.5. Tracks of charged particles in a bubble chamber. Also seen are δ electrons produced by interactions of the incident particles in the bubble-chamber liquid, which are spiralling in the transverse magnetic field [18].

with high precision since the spatial resolution of bubble chambers is excellent. Furthermore, the bubble density along the track is proportional to the energy loss $\mathrm{d}E/\mathrm{d}x$ by ionisation. For $p/m_0c = \beta\gamma \ll 4$ the energy loss can be approximated by

$$\frac{\mathrm{d}E}{\mathrm{d}x} \propto \frac{1}{\beta^2} \ . \tag{6.1}$$

If the momentum of the particle is known and if the velocity is determined from an energy-loss measurement, the particle can be identified.

Figure 6.5 shows tracks of charged particles in a bubble chamber. One can see the decay of a neutral particle producing a 'V' (presumably

https://doi.org/10.1017/9781009401531.009 Published online by Cambridge University Press

Table 6.1. *Characteristic properties of bubble-chamber liquids [5, 19]*

Bubble-chamber filling	Boiling point T [K]	Vapour pressure [bar]	Density [g/cm^3]	Radiation length X_0 [cm]	Nuclear interaction length λ_I [cm]
^{4}He	3.2	0.4	0.14	1027	437
$^1H_2$	26	4	0.06	1000	887
D_2	30	4.5	0.14	900	403
^{20}Ne	36	7.7	1.02	27	89
C_3H_8	333	21	0.43	110	176
CF_3Br (Freon)	303	18	1.5	11	73

$K^0 \rightarrow \pi^+ + \pi^-$) and δ electrons spiralling in the transverse magnetic field.

For the investigation of photoproduction on protons naturally, the best choice is a pure hydrogen filling. Results on photoproduction off neutrons can be obtained from D_2 fillings, because no pure neutron liquid exists (maybe with the exception of neutron stars). The photonuclear cross section on neutrons can be determined according to

$$\sigma(\gamma, n) = \sigma(\gamma, d) - \sigma(\gamma, p) \ . \tag{6.2}$$

If, e.g., the production of neutral pions is to be investigated, a bubble-chamber filling with a small radiation length X_0 is required, because the π^0 decays in two photons which have to be detected via the formation of electromagnetic showers. In this case, xenon or Freon can be chosen as chamber gas.

Table 6.1 lists some important gas fillings for bubble chambers along with their characteristic parameters [5, 19].

If one wants to study nuclear interactions with bubble chambers, the nuclear interaction length λ_I should be as small as possible. In this case heavy liquids like Freon are indicated.

Bubble chambers are an excellent device if the main purpose of the experiment is to analyse complex and rare events. For example, the Ω^- – after first hints from experiments in cosmic rays – could be unambiguously discovered in a bubble-chamber experiment.

In recent times the application of bubble chambers has, however, been superseded by other detectors like electronic devices. The reasons for this

originate from some serious intrinsic drawbacks of the bubble chamber listed as follows:

- Bubble chambers cannot be triggered.
- They cannot be used in storage-ring experiments because it is difficult to achieve a 4π geometry with this type of detector. Also the 'thick' entrance windows required for the pressure container prevents good momentum resolution because of multiple scattering.
- For high energies the bubble chamber is not sufficiently massive to stop the produced particles. This precludes an electron and hadron calorimetry – not to mention the difficult and tedious analysis of these cascades – because shower particles will escape from the detector volume.
- The identification of muons with momenta above several GeV/c in the bubble chamber is impossible because they look almost exactly like pions as far as the specific energy loss is concerned. Only by use of additional detectors (external muon counters) a π/μ separation can be achieved.
- The lever arm of the magnetic field is generally insufficient for an accurate momentum determination of high-momentum particles.
- Experiments which require high statistics are not really practical because of the time-consuming analysis of bubble-chamber pictures.

However, bubble chambers are still used in experiments with external targets (fixed-target experiments) and in non-accelerator experiments. Because of their high intrinsic spatial resolution of several micrometre, bubble chambers can serve as vertex detectors in these experiments [20, 21].

To be able to measure short lifetimes in bubble chambers the size of the bubbles must be limited. This means that the event under investigation must be photographed relatively soon after the onset of bubble formation when the bubble size is relatively small, thereby guaranteeing a good spatial resolution and, as a consequence, also good time resolution. In any case the bubble size must be small compared to the decay length of the particle.

By use of the technique of holographic recording a three-dimensional event reconstruction can be achieved [22]. With these high-resolution bubble chambers, e.g., the lifetimes of short-lived particles can be determined precisely. For a spatial resolution of $\sigma_x = 6\,\mu\text{m}$ decay-time measurement errors of

https://doi.org/10.1017/9781009401531.009 Published online by Cambridge University Press

$$\sigma_\tau = \frac{\sigma_x}{c} = 2 \cdot 10^{-14}\,\mathrm{s} \tag{6.3}$$

are reachable.

Bubble chambers have contributed significantly to the field of high-energy hadron collisions and neutrino interactions [23].

6.3 Streamer chambers

In contrast to streamer *tubes*, which represent a particular mode of operation for special cylindrical counters, streamer *chambers* are large-volume detectors in which events are normally recorded photographically [24–28]. In streamer chambers the volume between two planar electrodes is filled with a counting gas. After passage of a charged particle, a high-voltage pulse of high amplitude, short rise time and limited duration is applied to the electrodes. Figure 6.6 sketches the principle of operation of such a detector.

In the most frequent mode of operation, particles are incident approximately perpendicular to the electric field into the chamber. Each individual ionisation electron will start an avalanche in the homogeneous, very strong electric field in the direction of the anode. Since the electric field is time-dependent (amplitude of the high-voltage pulse $\approx 500\,\mathrm{kV}$, rise and decay time $\approx 1\,\mathrm{ns}$, pulse duration: several ns), the avalanche formation is interrupted after the decay time of the high-voltage pulse. The high amplitude of the voltage pulse leads to large gas amplifications ($\approx 10^8$) like in streamer tubes; however, the streamers can only extend over a very small region of space. Naturally, in the course of the avalanche development large numbers of gas atoms are excited and subsequently de-excite, leading to light emission. Luminous streamers are formed. Normally, these streamers are not photographed in the side view as sketched in Fig. 6.6, but through one electrode which can be made from a transparent wire mesh. In this projection the longish streamers appear as luminous dots characterising the track of the charged particle.

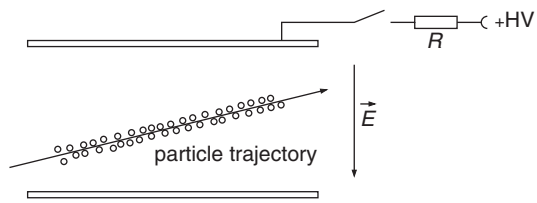

Fig. 6.6. Principle of construction of a streamer chamber.

https://doi.org/10.1017/9781009401531.009 Published online by Cambridge University Press

The art of the operation of streamer chambers lies in the production of a high-voltage signal with the required properties. The rise time must be extremely short (ns), otherwise the leading edge of the pulse would displace the ionisation electrons from the original track. A slow leading edge of the pulse would act as a clearing field resulting in a displacement of the particle track. Streamer development proceeds in very large electric fields ($\approx 30\,\mathrm{kV/cm}$). It must, however, be interrupted after a short time, so that the streamers will not grow too large or even produce a spark. Streamers that are too large imply a poor spatial resolution. A suitable high-voltage pulse can be obtained using a Marx generator connected by a suitable circuit (*transmission line*, Blumlein circuit, spark gaps) to the streamer chamber providing short signals of high amplitude [24, 26].

For fast repetition rates the large number of electrons produced in the course of streamer formation poses a problem. It would take too long a time to remove these electrons from the chamber volume by means of a clearing field. Therefore, electronegative components are added to the counting gas to which the electrons are attached. *Electronegative quenchers* like SF_6 or SO_2 have proven to be good. These quenchers allow cycle times of several 100 ms. The positive ions produced during streamer formation do not present a problem because they can never start new streamer discharges due to their low mobility.

Streamer chambers provide pictures of excellent quality. Also targets can be mounted in the chamber to obtain the interaction vertex in the sensitive volume of the detector.

Figure 6.7 shows the interaction of an antiproton with a neon nucleus in a streamer chamber in which – among others – a positive pion is produced.

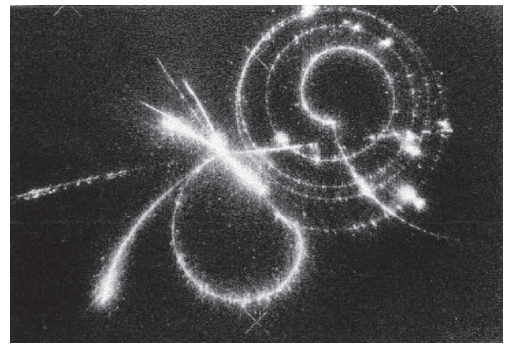

Fig. 6.7. Interaction of an antiproton with a neon nucleus in a streamer chamber producing – among others – a positive pion which decays into a muon yielding eventually a positron which escapes from the chamber [18].

https://doi.org/10.1017/9781009401531.009 Published online by Cambridge University Press

This π^+ spirals anticlockwise and decays into a muon, which also spirals in the transverse magnetic field and eventually decays into a positron, which escapes from the chamber [18].

In a different mode of operation of the streamer chamber, particles are incident within $\pm 30°$ with respect to the electric field into the detector. Exactly as mentioned before, very short streamers will develop which now, however, merge into one another and form a plasma channel along the particle track. (This variant of the streamer chamber is also called *track spark chamber* [8, 28].) Since the high-voltage pulse is very short, no spark between the electrodes develops. Consequently, only a very low current is drawn from the electrodes [5, 8, 24].

Streamer chambers are well suited for the recording of complex events; they have, however, the disadvantage of a time-consuming analysis.

6.4 Neon-flash-tube chamber

The *neon-flash-tube chamber* is also a discharge chamber [17, 29–32]. Neon- or neon/helium-filled glass tubes (at atmospheric pressure), glass spheres (*Conversi tubes*) or polypropylene-extruded plastic tubes with rectangular cross section are placed between two metal electrodes (Fig. 6.8).

After a charged particle has passed through the neon-flash-tube stack, a high-voltage pulse is applied to the electrodes that initiates a gas discharge in those tubes, which have been passed by the particle. This gas discharge propagates along the total length of the tube and leads to a glow discharge in the whole tube. Typical tube lengths are around 2 m with diameters between 5 mm and 10 mm. The glow discharge can be intensified by afterpulsing with high voltage so that the flash tubes can be photographed end on. But purely electronic recording with the help of pickup electrodes at the faces of the neon tubes can also be applied ('Ayre–Thompson technique' [33, 34]). These pickup electrodes supply large signals which can be directly processed without additional preamplifiers.

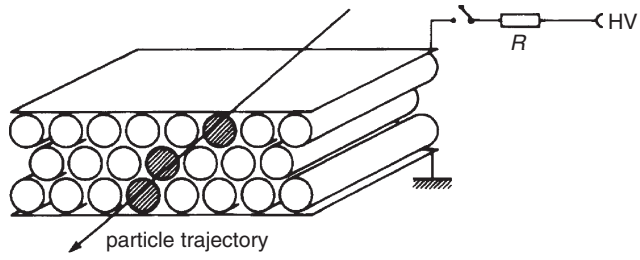

Fig. 6.8. Working principle of a neon-flash-tube chamber.

https://doi.org/10.1017/9781009401531.009 Published online by Cambridge University Press

Fig. 6.9. Shower of parallel muons in a flash-tube chamber [35, 36].

Depending on the tube diameter, spatial resolutions of several millimetres can be obtained. The memory time of this detector lies in the range around 20 μs; the dead time, however, is rather long at 30–1000 ms. For reasons of geometry, caused by the tube walls, the efficiency of one layer of neon flash tubes is limited to ≈ 80%. To obtain three-dimensional coordinates crossed layers of neon flash tubes are required.

Because of the relatively long dead time of this detector it was mainly used in cosmic-ray experiments, in the search for nucleon decay or in neutrino experiments. Figure 6.9 shows a shower of parallel cosmic-ray muons in a neon-flash-tube chamber [35, 36]. In Fig. 6.10 a single muon track is seen in an eight-layer stack of polypropylene-extruded plastic tubes [37].

A variant of the neon flash tube is the spherical Conversi tube [30, 31]. These are spherical neon tubes of approximately 1 cm diameter. Layers of Conversi tubes arranged in a matrix between two electrodes, one of which being made as a transparent grid, have been used to measure the lateral distribution of particles in extensive-air-shower experiments [8, 38].

6.5 Spark chambers

Before multiwire proportional and drift chambers were invented, the *spark chamber* was the most commonly used track detector which could be triggered ([8, 17, 39–43], and references in [17]).

https://doi.org/10.1017/9781009401531.009 Published online by Cambridge University Press

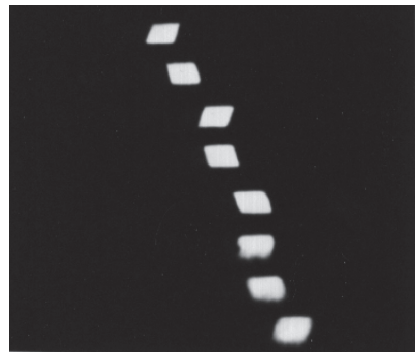

Fig. 6.10. Single muon track in a stack of polypropylene-extruded plastic tubes. Such extruded plastic tubes are very cheap since they are normally used as packing material. Because they have not been made for particle tracking, their structure is somewhat irregular, which can clearly be seen [37].

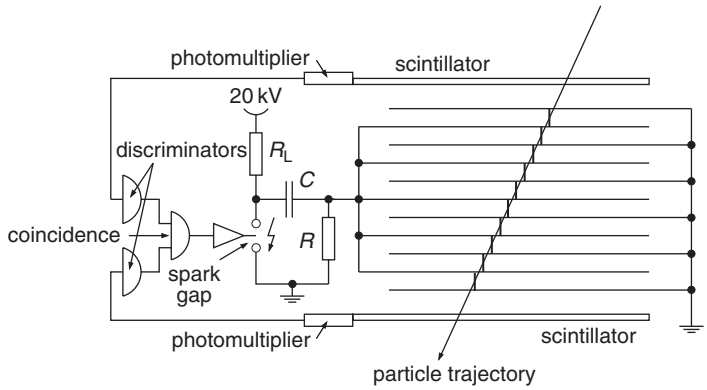

Fig. 6.11. Principle of operation of a multiplate spark chamber.

In a spark chamber a number of parallel plates are mounted in a gas-filled volume. Typically, a mixture of helium and neon is used as counting gas. Alternatingly, the plates are either grounded or connected to a high-voltage supply (Fig. 6.11). The high-voltage pulse is normally triggered to every second electrode by a coincidence between two scintillation counters placed above and below the spark chamber. The gas amplification is chosen in such a way that a spark discharge occurs at the point of the passage of the particle. This is obtained for gas amplifications between 10^8 and 10^9. For lower gas amplifications sparks will not develop, while for larger gas amplifications sparking at unwanted positions (e.g. at spacers which separate the plates) can occur. The discharge channel follows the electric field. Up to an angle of 30° the conducting plasma channel can, however, follow the particle trajectory [8] as in the track spark chamber.

https://doi.org/10.1017/9781009401531.009 Published online by Cambridge University Press

Between two discharges the produced ions are removed from the detector volume by means of a *clearing field*. If the time delay between the passage of the particle and the high-voltage signal is less than the memory time of about 100 μs, the efficiency of the spark chamber is close to 100%. A clearing field, of course, removes also the primary ionisation from the detector volume. For this reason the time delay between the passage of the particle and the application of the high-voltage signal has to be chosen as short as possible to reach full efficiency. Also the rise time of the high-voltage pulse must be short because otherwise the leading edge acts as a clearing field before the critical field strength for spark formation is reached.

Figure 6.12 shows the track of a cosmic-ray muon in a multiplate spark chamber [5, 44].

If several particles penetrate the chamber simultaneously, the probability that all particles will form a spark trail decreases drastically with increasing number of particles. This is caused by the fact that the first spark discharges the charging capacitor to a large extent so that less voltage or energy, respectively, is available for the formation of further sparks. This problem can be solved by limiting the current drawn by a spark. In *current-limited spark chambers* partially conducting glass plates are mounted in front of the metallic electrodes which prevent a high-current spark discharge. In such glass spark chambers a high multitrack efficiency can be obtained [45, 46].

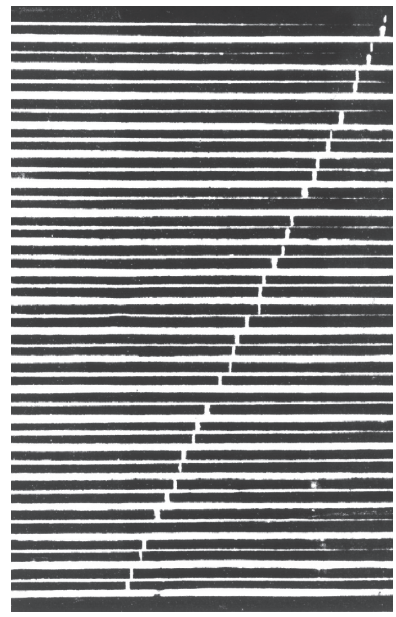

Fig. 6.12. Track of a cosmic-ray muon in a multiplate spark chamber [44].

https://doi.org/10.1017/9781009401531.009 Published online by Cambridge University Press

Apart from the photographic recording in spark chambers, which has to be made stereoscopically to allow three-dimensional event reconstruction, a purely electronic readout is also possible.

If the electrodes are made from layers of wires, the track coordinate can be obtained like in the multiwire proportional chamber by identifying the discharged wire. This method would require a large number of wires to obtain a high spatial resolution. On the other hand, the track reconstruction can be simplified with the help of a *magnetostrictive readout*.

The spark discharge represents a time-dependent current $\mathrm{d}I/\mathrm{d}t$. The current signal propagates along the chamber wire and reaches a *magnetostrictive delay line* stretched perpendicular to the chamber wires. This magnetostrictive delay line is positioned directly on the chamber wires without having ohmic contact to them. The current signal, along with its associated time-dependent magnetic field $\mathrm{d}\vec{H}/\mathrm{d}t$, produces in the magnetostrictive delay line a magnetostriction, i.e. a local variation of the length, which propagates in time and space with its characteristic velocity of sound. In a pickup coil at the end of the magnetostrictive delay line the mechanical signal of magnetostriction is converted back into a time-dependent magnetic-field signal $\mathrm{d}\vec{H}/\mathrm{d}t$ leading to a detectable voltage pulse. The measurement of the propagation time of the sound wave on the magnetostrictive delay line can be used to identify the number and hence the spatial coordinate of the discharged wire. Typical sound velocities of $\approx 5\,\mathrm{km/s}$ lead to spatial resolutions on the order of $200\,\mu\mathrm{m}$ [8, 47].

A somewhat older method of identifying discharged wires in wire spark chambers uses *ferrite cores* to localise the discharged wire. In this method each chamber wire runs through a small ferrite core [8]. The ferrite core is in a well-defined state. A discharging spark-chamber wire causes the ferrite core to flip. The state of ferrite cores is recorded by a readout wire. After reading out the event the flipped ferrite cores are reset into the initial state by a reset wire.

For all spark-chamber types a clearing field is necessary to remove the positive ions from the detector volume. This causes dead times of several milliseconds.

6.6 Nuclear emulsions

Tracks of charged particles in *nuclear emulsions* can be recorded by the photographic method [48–52]. Nuclear emulsions consist of fine-grained silver-halide crystals (AgBr and AgCl), which are embedded in a gelatine substrate. A charged particle produces a latent image in the emulsion. Due to the free charge carriers liberated in the ionisation process, some halide molecules are reduced to metallic silver in the emulsion.

https://doi.org/10.1017/9781009401531.009 Published online by Cambridge University Press

In the subsequent development process the silver-halide crystals are chemically reduced. This affects preferentially those microcrystals (nuclei) which are already disturbed and partly reduced. These are transformed into elemental silver. The process of fixation dissolves the remaining silver halide and removes it. Thereby the charge image, which has been transformed into elemental silver particles, remains stable.

The evaluation of the emulsion is usually done under a microscope by eye, but it can also be performed by using a Charge-Coupled Device (CCD) camera and a semi-automatic pattern-recognition device. Fully automated emulsion-analysis systems have also been developed [53].

The sensitivity of the nuclear emulsion must be high enough so that the energy loss of minimum-ionising particles is sufficient to produce individual silver-halide microcrystals along the track of a particle. Usually commercially available photoemulsions do not have this property. Furthermore, the silver grains which form the track and also the silver-halide microcrystals must be sufficiently small to enable a high spatial resolution. The requirements of high sensitivity and low grain size are in conflict and, therefore, demand a compromise. In most nuclear emulsions the silver grains have a size of $0.1\,\mu\mathrm{m}$ to $0.2\,\mu\mathrm{m}$ and so are much smaller than in commercial films (1–$10\,\mu\mathrm{m}$). The mass fraction of the silver halide (mostly AgBr) in the emulsion amounts to approximately 80%.

A typical thickness of emulsions is 20 to 1000 microns with sizes up to $50\,\mathrm{cm} \times 50\,\mathrm{cm}$. In the developing, fixing, washing and drying process extreme care must be taken not to lose the intrinsically high space resolution. In particular, a possible shrinking of the emulsion must be well understood.

Because of the high density of the emulsion ($\varrho = 3.8\,\mathrm{g/cm^3}$) and the related short radiation length ($X_0 = 2.9\,\mathrm{cm}$), stacks of nuclear emulsions are perfectly suited to detect electromagnetic cascades. On the other hand, hadron cascades hardly develop in such stacks because of the much larger nuclear interaction length ($\lambda_\mathrm{I} = 35\,\mathrm{cm}$).

The efficiency of emulsions for single or multiple particle passages is close to 100%. Emulsions are permanently sensitive but they cannot be triggered. They have been, and still are, in use in many cosmic-ray experiments [51]. They are, however, also suited for accelerator experiments as vertex detectors with high spatial resolution ($\sigma_x \approx 2\,\mu\mathrm{m}$) for the investigation of decays of short-lived particles.

The high resolution of complex events with large multiplicities is clearly shown in the interaction of a $228.5\,\mathrm{GeV}$ uranium nucleus in a nuclear emulsion (Fig. 6.13) [54].

Figure 6.14 shows the ionisation profile of an iron nucleus and a heavy nucleus ($Z \approx 90$) in a nuclear emulsion [55].

https://doi.org/10.1017/9781009401531.009 Published online by Cambridge University Press

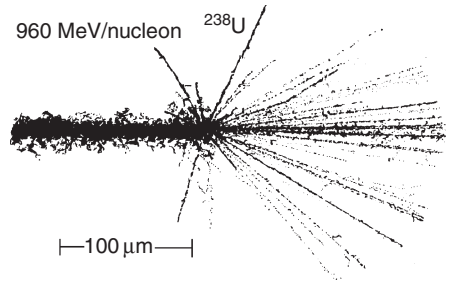

Fig. 6.13. Interaction of an uranium nucleus of energy 228.5 GeV in a nuclear emulsion [54].

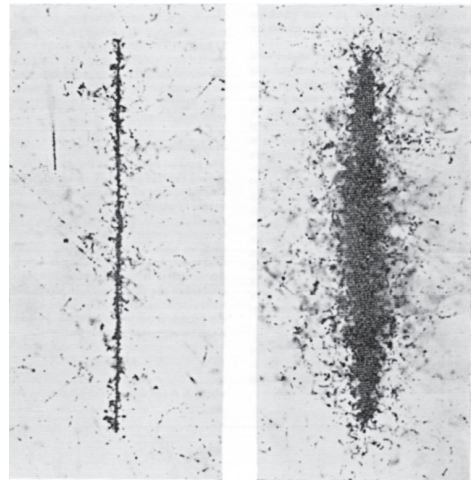

Fig. 6.14. Ionisation profile of an iron nucleus and a heavy nucleus ($Z \approx 90$) in a nuclear emulsion [55].

Occasionally, nuclear emulsions are used in accelerator experiments where extremely high spatial resolution is needed for rare events, like in the search for the tau neutrino (see Chap. 10 on 'Neutrino detectors').

Among others, the emulsion technique has contributed significantly in past decades to the fields of cosmic-ray physics, high-energy heavy-ion collisions, hypernuclear physics, neutrino oscillations, and to the study of charm and bottom particles [56].

6.7 Silver-halide crystals

The disadvantage of nuclear emulsions is that the sensitive volume of the detector is usually very small. The production of large-area *AgCl crystals* has been made possible several years ago. This has allowed the

https://doi.org/10.1017/9781009401531.009 Published online by Cambridge University Press

construction of another passive detector similar to emulsions. Charged particles produce Ag^+ ions and electrons along their track in a AgCl crystal. The mobility of Ag^+ ions in the lattice is very limited. They usually occupy positions between regular lattice atoms thereby forming a lattice defect. Free electrons from the conduction band reduce the Ag^+ ions to metallic silver. These Ag atoms attach further Ag^+ ions: the formation of silver clusters starts. To stabilise these silver clusters the crystal must be illuminated during or shortly after the passage of the particle providing the free electrons required for the reduction of the Ag^+ ions (storage or *conservation of particle tracks*). This is frequently done by using light with a wavelength of around 600 nm [57]. If this illumination is not done during data taking, the tracks will fade away. In principle, this illumination can also be triggered by an external signal which would allow the separation of interesting events from background. To this extent, the event recording in an AgCl crystal – in contrast to nuclear emulsions or plastic detectors – can be triggered.

Even in the unirradiated state there are a certain number of Ag ions occupying places between the regular lattice positions. A small admixture of cadmium chloride serves to reduce this unwanted silver concentration. This minimises the formation of background silver nuclei on lattice defects, thereby decreasing the 'noise' in AgCl crystals.

To allow the Ag clusters to grow to microscopically visible size, the AgCl crystal is irradiated by short-wavelength light during the development process. This provides further free electrons in the conduction band which in turn will help to reduce the Ag^+ ions as they attach themselves to the already existing clusters.

This process of track amplification (*decoration*) produces a stable track which can then be evaluated under a microscope.

Silver-chloride detectors show – just like plastic detectors – a certain threshold effect. The energy loss of relativistic protons is too small to produce tracks which can be developed in the crystal. The AgCl detector, however, is well suited to measure tracks of heavy nuclei ($Z \geq 3$).

The tedious evaluation of nuclear tracks under a microscope can be replaced by automatic pattern-recognition methods similar to those which are in use for nuclear emulsions and plastic detectors [58–60]. The spatial resolution which can be achieved in AgCl crystals is comparable to that of nuclear emulsions.

6.8 X-ray films

Emulsion chambers, i.e. stacks of nuclear emulsions when used in cosmic-ray experiments, are frequently equipped with additional large-area *X-ray*

https://doi.org/10.1017/9781009401531.009 Published online by Cambridge University Press

films [61–63]. The main differences of the X-ray films from nuclear emulsions are the low grain size from 50 nm to 200 nm (0.05–0.2 microns) at a thickness of 7–20 microns [64]. These industrial X-ray films allow the detection of high-energy electromagnetic cascades (see Chap. 8 on 'Calorimetry') and the determination of the energy of electrons or photons initiating these cascades by photometric methods. This is done by constructing a stack of X-ray films alternating with thin lead sheets. The longitudinal and lateral development of electromagnetic cascades can be inferred from the structure of the darkness in the X-ray films.

X-ray films employed in cosmic-ray experiments are mainly used for the detection of photons and electrons in the TeV range. Hadronic cascades are harder to detect in stacks with X-ray films. They can, however, be recorded via the π^0 fraction in the hadron shower ($\pi^0 \rightarrow \gamma\gamma$). This is related to the fact that photons and electrons initiate narrowly collimated cascades producing dark spots on the X-ray film, whereas hadronic cascades, because of the relatively large transverse momenta of secondary particles, spread out over a larger area on the film thus not exceeding the threshold required for a blackening of the film.

Saturation effects in the region of the maximum of shower development (central blackening) cause the relation between the deposited energy E and the photometrically measured blackening D not to be linear [64]. For typical X-ray films which are used in the TeV range one gets

$$D \propto E^{0.85} \quad . \tag{6.4}$$

The radial distribution of the blackening allows the determination of the point of particle passage with relatively high precision.

6.9 Thermoluminescence detectors

Thermoluminescence detectors are used in the field of radiation protection [65–67] and also in cosmic-ray experiments.

Particle detection in thermoluminescence detectors is based on the fact that in certain crystals ionising radiation causes electrons to be transferred from the valence band to the conduction band where they may occupy stable energy states [68]. In the field of radiation protection, media, which retain the dose information, such as manganese- or titanium-activated calcium-fluoride (CaF_2) or lithium-fluoride (LiF) crystals, are used. The stored energy caused by irradiating the crystal is proportional to the absorbed dose. Heating the thermoluminescence dosimeter to a temperature between 200 °C and 400 °C can liberate this energy by emission of photons. The number of produced photons is proportional to the absorbed energy dose.

In cosmic-ray experiments thermoluminescence films (similar to X-ray films) are used for the measurement of high-energy electromagnetic cascades. A thermoluminescence detector is made by coating a glass or metal surface with a layer of thermoluminescent powder. The smaller the grain size of microcrystals on the film the better the spatial resolution that can be reached. The ionising particles in the electron cascade produce stable thermoluminescence centres. The determination of where the energy is deposited on the film can be achieved by scanning the film with an infrared laser. During the process of scanning the intensity of emitted photons must be measured with a photomultiplier. If the spatial resolution is not limited by the radial extension of the laser spot, resolutions on the order of a few micrometres can be obtained [69].

Apart from doped calcium-fluoride or lithium-fluoride crystals and storage phosphors, which are commonly used in the field of radiation protection, cosmic-ray experiments utilise mainly $BaSO_4$, Mg_2SiO_4 and $CaSO_4$ as thermoluminescent agents. While thermoluminescence dosimeters measure the integrated absorbed energy dose, in cosmic-ray experiments the measurement of individual events is necessary.

In such experiments thermoluminescence films are stacked similar to X-ray films or emulsions alternatingly with lead-absorber sheets. The hadrons, photons or electrons to be detected initiate hadronic or electromagnetic cascades in the thermoluminescence calorimeter. Neutral pions produced in hadronic cascades decay relatively quickly (in $\approx 10^{-16}$ s) into two photons thereby initiating electromagnetic subcascades.

In contrast to hadronic cascades with a relatively large lateral width, the energy in electromagnetic cascades is deposited in a relatively small region thereby enabling a recording of these showers. That is why electromagnetic cascades are directly measured in such a detector type while hadronic cascades are detected only via their π^0 content. Thermoluminescence detectors exhibit an energy threshold for the detection of particles. This threshold is approximately 1 TeV per event in europium-doped $BaSO_4$ films [69].

6.10 Radiophotoluminescence detectors

Silver-activated phosphate glass, after having been exposed to ionising radiation, emits fluorescence radiation in a certain frequency range if irradiated by ultraviolet light. The intensity of the fluorescence radiation is a measure for the energy deposition by the ionising radiation. The Ag^+ ions produced by ionising particles in the glass represent stable photoluminescence centres. Reading out the energy deposition with ultraviolet light does not erase the information of the energy loss in the

https://doi.org/10.1017/9781009401531.009 Published online by Cambridge University Press

detector [68]. *Yokota glass* is mostly used in these phosphate-glass detectors. It consists of 45% $AlPO_3$, 45% $LiPO_3$, 7.3% $AgPO_3$ and 2.7% B_2O_3 and has a typical density of 2.6 g/cm^3 for a silver mass fraction of 3.7%. Such phosphate-glass detectors are mainly used in the field of radiation protection for dosimetric measurements.

By scanning a two-dimensional radiophotoluminescence sheet with a UV laser, it is possible to determine the spatial dependence of the energy deposit by measuring the position-dependent fluorescence light yield. If individual events are recorded, a threshold energy on the order of 1 TeV is required just as in thermoluminescence detectors. The spatial resolution that can be obtained is limited also in this case by the resolution of the scanning system.

6.11 Plastic detectors

Particles of high electric charge destroy the local structure in a solid along their tracks. This local destruction can be intensified by etching and thereby made visible. Solids such as inorganic crystals, glasses, plastics, minerals or even metals can be used for this purpose [70–74]. The damaged parts of the material react with the etching agent more intensively than the undamaged material and characteristic *etch cones* will be formed.

If the *etching process* is not interrupted, the etch cones starting from the surface of the plastic will merge and form a hole at the point of the particle track. The etching procedure will also remove some part of the surface material.

Figure 6.15 [75] shows a microphotograph of tracks made in a CR-39 *plastic nuclear-track detector* exposed on board the Mir Space Station during a NASA mission. The width of the track at the centre is approximately 15 µm [75].

For inclined incidence the etch cones exhibit an elliptical form.

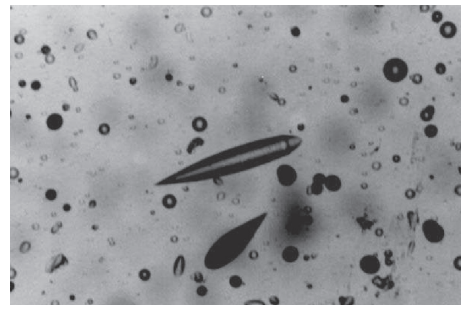

Fig. 6.15. Microphotograph of cosmic-ray tracks in a plastic nuclear-track detector. Typical track widths are on the order of 10 µm [75].

https://doi.org/10.1017/9781009401531.009 Published online by Cambridge University Press

The determination of the energy of heavy ions is frequently done in stacks containing a large number of foils. The radiation damage of the material – just as the energy loss of charged particles – is proportional to the square of their charge, and depends also on the velocity of the particles.

Plastic detectors show a threshold effect: the minimum radiation damage caused by protons and α particles is frequently insufficient to produce etchable tracks. The detection and measurement of heavy ions, e.g. in primary cosmic rays ($Z \geq 3$), will consequently not be disturbed by a high background of protons and α particles. The size of the etch cones (for a fixed etching time) is a measure of the energy loss of the particles. It allows, therefore, if the velocity of the particles is known, a determination of the charge of the nuclei. A stack of plastic detectors, flown in a balloon in a residual atmosphere of several grams per square centimetre, thus permits a determination of the elemental abundance in primary cosmic rays.

Plastic detectors are also utilised in the search for magnetic monopoles which, according to theory, should cause strong ionisation. Such experiments can also be performed on proton storage rings because the high background of singly charged particles does not impair the search for monopoles due to the threshold behaviour of the plastic material.

In a similar way to plastic detectors, minerals also conserve a local radiation damage over a long period of time. This leads to the possibility of dating uranium-containing minerals by counting the number of spontaneous fission events. If the minerals are time calibrated in this way, the number of tracks initiated by cosmic radiation in these minerals indicates that the intensity of cosmic rays has not varied significantly ($\leq 10\%$) over the past 10^6 years [76, 77].

The evaluation of plastic detectors under the microscope is very tiresome. The information on particle tracks in a plastic sheet can, however, also be digitised by means of a CCD camera looking through a microscope onto the foil. The digitised event is subsequently processed with a programme for automatic pattern reconstruction [74].

A nuclear detector with super-high spatial resolution is provided, for example, by a small chip of MoS_2. High-energy nuclei penetrating the MoS_2 sample produce craters on its surface due to local radiation damage. Analysing these craters by scanning tunnelling microscopy allows spatial resolutions on the order of 10 Å and two-track resolutions of 30–50 Å [78].

6.12 Problems

6.1 The saturation vapour pressure p_r over a spherical surface of radius r is larger compared to the corresponding pressure p_∞ over a planar surface. To achieve good quality tracks in a cloud chamber one

https://doi.org/10.1017/9781009401531.009 Published online by Cambridge University Press

has to aim for $p_r/p_\infty = 1.001$. What kind of droplet size results from this condition in a cloud chamber with air and water vapour (air and alcohol vapour)?

The surface tension for water (alcohol) is 72.8 dyn/cm (22.3 dyn/cm).

6.2 In a discharge chamber the gas multiplication is characterised by the first Townsend coefficient α which describes the increase of the electron number $\mathrm{d}n/\mathrm{d}x$ per primary electron over the distance $\mathrm{d}x$.

$$\mathrm{d}n = \alpha n \, \mathrm{d}x \ .$$

On the other hand, some of the electrons can be attached to electronegative gases in the chamber (attachment coefficient β).

Work out the number of electrons and negative ions on a multiplication distance d and the total charge increase $(n_e + n_{\mathrm{ion}})/n_0$, where n_0 is the primary ionisation ($n_0 = 100/\mathrm{cm}, \alpha = 20/\mathrm{cm}, \beta = 2/\mathrm{cm}, d = 1\,\mathrm{cm}$).

6.3 In a nuclear emulsion ($X_0 = 5\,\mathrm{cm}$) of 500 µm thickness an average projected scattering angle for electrons is found to be $\sqrt{\langle\theta^2\rangle} = 5°$. Work out the electron momentum.

References

[1] C.T.R. Wilson, On a Method of Making Visible the Paths of Ionizing Particles, *Proc. R. Soc. Lond.* **A85** (1911) 285–8; Expansion Apparatus for Making Visible the Tracks of Ionizing Particles in Gases: Results Obtained, *Proc. R. Soc. Lond.* **A87** (1912) 277–92

[2] C.T.R. Wilson, Uranium Rays and Condensation of Water Vapor, *Cambridge Phil. Soc. Proc.* **9** (1897) 333–6; *Phil. Trans. R. Soc. Lond.* **189** (1897) 265–8; On the Condensation Nuclei Produced in Gases by the Action of Röntgen Rays, Uranium Rays, Ultra-Violet Light, and Other Agents, *Proc. R. Soc. Lond.* **64** (1898–9), 127–9

[3] C.M. York, Cloud Chambers, in S. Flügge (ed.), *Handbuch der Physik*, Band **XLV**, Springer, Berlin (1958) 260–313

[4] G.D. Rochester & J.G. Wilson, *Cloud Chamber Photographs of Cosmic Radiation*, Pergamon Press, London (1952)

[5] O.C. Allkofer, *Teilchendetektoren*, Thiemig, München (1971)

[6] W. Wolter, private communication (1969)

[7] U. Wiemken, *Untersuchungen zur Existenz von Quarks in der Nähe der Kerne Großer Luftschauer mit Hilfe einer Nebelkammer*, Ph.D. Thesis, University of Kiel; U. Wiemken, Diploma Thesis, University of Kiel (1972); K. Sauerland, private communication (1993)

[8] O.C. Allkofer, W.D. Dau & C. Grupen, *Spark Chambers*, Thiemig, München (1969)

[9] A. Langsdorf, A Continuously Sensitive Cloud Chamber, *Phys. Rev.* **49** (1936) 422–34; *Rev. Sci. Instr.* **10** (1939) 91–103
[10] V.K. Ljapidevski, Die Diffusionsnebelkammer, *Fortschr. der Physik* **7** (1959) 481–500
[11] E.W. Cowan, Continuously Sensitive Diffusion Cloud Chamber, *Rev. Sci. Instr.* **21** (1950) 991–6
[12] D.A. Glaser, Some Effects of Ionizing Radiation on the Formation of Bubbles in Liquids, *Phys. Rev.* **87** (1952) 665
[13] D.A. Glaser, Bubble Chamber Tracks of Penetrating Cosmic Ray Particles, *Phys. Rev.* **91** (1953) 762–3
[14] D.A. Glaser, Progress Report on the Development of Bubble Chambers, *Nuovo Cim. Suppl.* **2** (1954) 361–4
[15] D.A. Glaser, The Bubble Chamber, in S. Flügge (ed.), *Handbuch der Physik*, Band **XLV**, Springer, Berlin (1958) 314–41
[16] L. Betelli *et al.*, *Particle Physics with Bubble Chamber Photographs*, CERN/INFN-Preprint (1993)
[17] P. Galison, *Bubbles, Sparks and the Postwar Laboratory*, Proc. Batavia Conf. 1985, *Pions to Quarks* (1989) 213–51
[18] CERN Photo Archive
[19] K. Kleinknecht, *Detectors for Particle Radiation*, 2nd edition, Cambridge University Press, Cambridge (1998); *Detektoren für Teilchenstrahlung*, Teubner, Wiesbaden (2005)
[20] W.J. Bolte *et al.*, A Bubble Chamber for Dark Matter Detection (the COUPP project status), *J. Phys. Conf. Ser.* **39** (2006) 126–8
[21] Y.L. Ju, J.R. Dodd, W.J. Willis (Nevis Labs, Columbia U.) & L.X. Jia (Brookhaven), Cryogenic Design and Operation of Liquid Helium in Electron Bubble Chamber, *AIP Conf. Proc.* **823** (2006) 433–40
[22] H. Bingham *et al.*, *Holography of Particle Tracks in the Fermilab 15-Foot Bubble Chamber*, E-632 Collaboration, CERN-EF-90-3 (1990); *Nucl. Instr. Meth.* **A297** (1990) 364–89
[23] W. Kittel, *Bubble Chambers in High Energy Hadron Collisions*, Nijmegen Preprint HEN-365 (1993)
[24] P. Rice-Evans, *Spark, Streamer, Proportional and Drift Chambers*, Richelieu Press, London (1974)
[25] V. Eckardt, *Die Speicherung von Teilchenspuren in einer Streamerkammer*, Ph.D. Thesis, University of Hamburg (1971)
[26] F. Bulos *et al.*, *Streamer Chamber Development*, SLAC-Technical-Report, SLAC-R-74, UC-28 (1967)
[27] F. Rohrbach, *Streamer Chambers at CERN During the Past Decade and Visual Techniques of the Future*, CERN-EF-88-17 (1988)
[28] G. Charpak, Principes et Essais Préliminaires D'un Nouveau Détecteur Permettant De Photographier la Trajectoire des Particules Ionisantes Dans un Gas, *J. Phys. Rad.* **18** (1957) 539–47
[29] M. Conversi, *The Development of the Flash and Spark Chambers in the 1950's*, CERN-EP-82-167 (1982)

[30] M. Conversi & A. Gozzini, The 'Hodoscope Chamber': A New Instrument for Nuclear Research, *Nuovo Cim.* **2** (1955) 189–95
[31] M. Conversi *et al.*, A New Type of Hodoscope of High Spatial Resolution, *Nuovo Cim. Suppl.* **4** (1956) 234–9
[32] M. Conversi & L. Frederici, Flash Chambers of Plastic Material, *Nucl. Instr. Meth.* **151** (1978) 93–106
[33] C.A. Ayre & M.G. Thompson, Digitization of Neon Flash Tubes, *Nucl. Instr. Meth.* **69** (1969) 106–110
[34] C.G. Dalton & G.J. Krausse, Digital Readout for Flash Chambers, *Nucl. Instr. Meth.* **158** (1979) 289–97
[35] F. Ashton & J. King, The Electric Charge of Interacting Cosmic Ray Particles at Sea Level, *J. Phys.* **A4** (1971) L31–3
[36] F. Ashton, private communication (1991)
[37] J. Sonnemeyer, Staatsexamensarbeit, Universität Siegen (1979)
[38] J. Trümper, E. Böhm & M. Samorski, private communication (1969)
[39] J.W. Keuffel, Parallel Plate Counters, *Rev. Sci. Instr.* **20** (1949) 202–11
[40] S. Fukui & S. Miyamoto, A New Type of Particle Detector: The Discharge Chamber, *Nuovo Cim.* **11** (1959) 113–15
[41] O.C. Allkofer *et al.*, Die Ortsbestimmung geladener Teilchen mit Hilfe von Funkenzählern und ihre Anwendung auf die Messung der Vielfachstreuung von Mesonen in Blei, *Phys. Verh.* **6** (1955) 166–71; P.G. Henning, *Die Ortsbestimmung geladener Teilchen mit Hilfe von Funkenzählern*, Ph.D. Thesis, University of Hamburg (1955); *Atomkernenergie* **2** (1957) 81–9
[42] F. Bella, C. Franzinetti & D.W. Lee, On Spark Counters, *Nuovo Cim.* **10** (1953) 1338–40; F. Bella & C. Franzinetti, Spark Counters, *Nuovo Cim.* **10** (1953) 1461–79
[43] T.E. Cranshaw & J.F. De Beer, A Triggered Spark Counter, *Nuovo Cim.* **5** (1957) 1107–16
[44] V.S. Kaftanov & V.A. Liubimov, Spark Chamber Use in High Energy Physics, *Nucl. Instr. Meth.* **20** (1963) 195–202
[45] S. Attenberger, Spark Chamber with Multi-Track Capability, *Nucl. Instr. Meth.* **107** (1973) 605–10
[46] R. Kajikawa, Direct Measurement of Shower Electrons with 'Glass-Metal' Spark Chambers, *J. Phys. Soc. Jpn* **18** (1963) 1365–73
[47] A.S. Gavrilov *et al.*, Spark Chambers with the Recording of Information by Means of Magnetostrictive Lines, *Instr. Exp. Techn.* **6** (1966) 1355–63
[48] S. Kinoshita, Photographic Action of the α-Particles Emitted from Radio-Active Substances, *Proc. R. Soc. Lond.* **83** (1910) 432–53
[49] M.M. Shapiro, Nuclear Emulsions, in S. Flügge (ed.), *Handbuch der Physik*, Band **XLV**, Springer, Berlin (1958) 342–436
[50] R. Reinganum, Streuung und Photographische Wirkung der α-Strahlen, *Z. Phys.* **12** (1911) 1076–81
[51] D.H. Perkins, *Cosmic Ray Work with Emulsions in the 40's and 50's*, Oxford University Preprint OUNP 36/85 (1985)

[52] C.F. Powell, P.H. Fowler & D.H. Perkins, *The Study of Elementary Particles by the Photographic Method*, Pergamon Press, London (1959)
[53] S. Aoki *et al.*, Fully Automated Emulsion Analysis System, *Nucl. Instr. Meth.* **B51** (1990) 466–73
[54] M. Simon, Lawrence Berkeley Lab. XBL-829-11834, private communication (1992)
[55] G.D. Rochester, Atomic Nuclei From Outer Space, *British Association for the Advancement of Science* (December 1970) 183–94; G.D. Rochester & K.E. Turver, Cosmic Rays of Ultra-high Energy, *Contemp. Phys.* **22** (1981) 425–50; G.D. Rochester & A.W. Wolfendale, Cosmic Rays at Manchester and Durham, *Acta Phys. Hung.* **32** (1972) 99–114
[56] J. Sacton, *The Emulsion Technique and its Continued Use*, University of Brussels, Preprint IISN 0379-301X/IIHE-93.06 (1993)
[57] Th. Wendnagel, University of Frankfurt am Main, private communication (1991)
[58] C. Childs & L. Slifkin, Room Temperature Dislocation Decoration Inside Large Crystals, *Phys. Rev. Lett.* **5(11)** (1960) 502–3; A New Technique for Recording Heavy Primary Cosmic Radiation and Nuclear Processes in Silver Chloride Single Crystals, *IEEE Trans. Nucl. Sci.* **NS-9 (3)** (1962) 413–15
[59] Th. Wendnagel *et al.*, Properties and Technology of Monocrystalline AgCl-Detectors; 1. Aspects of Solid State Physics *and* Properties and Technology of AgCl-Detectors; 2. Experiments and Technological Performance, in S. Francois (ed.), *Proc. 10th Int. Conf. on SSNTD, Lyon 1979*, Pergamon Press, London (1980)
[60] A. Noll, *Methoden zur Automatischen Auswertung von Kernwechselwirkungen in Kernemulsionen und AgCl-Kristallen*, Ph.D. Thesis, University of Siegen (1990)
[61] C.M.G. Lattes, Y. Fujimoto & S. Hasegawa, *Hadronic Interactions of High Energy Cosmic Rays Observed by Emulsion Chambers*, ICR-Report-81-80-3, University of Tokyo (1980)
[62] Mt. Fuji Collaboration (M. Akashi *et al.*), *Energy Spectra of Atmospheric Cosmic Rays Observed with Emulsion Chambers*, ICR-Report-89-81-5, University of Tokyo (1981)
[63] J. Nishimura *et al.*, Emulsion Chamber Observations of Primary Cosmic Ray Electrons in the Energy Range 30–1000 GeV, *Astrophys. J.* **238** (1980) 394–409
[64] I. Ohta *et al.*, *Characteristics of X-Ray Films Used in Emulsion Chambers and Energy Determination of Cascade Showers by Photometric Methods*, 14th Int. Cosmic Ray Conf. München, Vol. 9, München (1975) 3154–9
[65] A.F. McKinley, *Thermoluminescence Dosimetry*, Adam Hilger Ltd, Bristol (1981)
[66] M. Oberhofer & A. Scharmann (eds.), *Applied Thermoluminescence Dosimetry*, Adam Hilger Ltd, Bristol (1981)
[67] Y.S. Horowitz, *Thermoluminescence and Thermoluminescent Dosimetry*, CRC Press (1984)

[68] E. Sauter, *Grundlagen des Strahlenschutzes*, Siemens AG, Berlin/München (1971); *Grundlagen des Strahlenschutzes*, Thiemig, München (1982)
[69] Y. Okamoto *et al.*, *Thermoluminescent Sheet to Detect the High Energy Electromagnetic Cascades*, 18th Int. Cosmic Ray Conf., Bangalore, Vol. 8 (1983) 161–5
[70] R.L. Fleischer, P.B. Price & R.M. Walker, *Nuclear Tracks in Solids; Principles and Application*, University of California Press, Berkeley (1975)
[71] P.H. Fowler & V.M. Clapham (eds.), *Solid State Nuclear Track Detectors*, Pergamon Press, Oxford (1982)
[72] F. Granzer, H. Paretzke & E. Schopper (eds.), *Solid State Nuclear Track Detectors*, Vols. 1 & 2, Pergamon Press, Oxford (1978)
[73] W. Enge, Introduction to Plastic Nuclear Track Detectors, *Nucl. Tracks* **4** (1980) 283–308
[74] W. Heinrich *et al.*, Application of Plastic Nuclear Track Detectors in Heavy Ion Physics, *Nucl. Tracks Rad. Measurements* **15(1–4)** (1988) 393–400
[75] Afzal Ahmed & Julie Oliveaux, Life Science Data Archive, Johnson Space Center, Houston (2005). web-page: http://lsda.jsc.nasa.gov/scripts/photoGallery/detail_result.cfm?image_id=1664
[76] M. Lang, U.A. Glasmacher, R. Neumann & G.A. Wagner, Etching Behaviour of Alpha-Recoil Tracks in Natural Dark Mica Studied via Artificial Ion Tracks, *Nucl. Instr. Meth.* **B209** (2003) 357–61
[77] J.A. Miller, J.A.C. Horsfall, N. Petford & R.H. Tizard, Counting Fission Tracks in Mica External Detectors, *Pure and Applied Geophysics*, **140(4)** (December 1993)
[78] T. Xiaowei *et al.*, A Nuclear Detector with Super-High Spatial Resolution, *Nucl. Instr. Meth.* **A320** (1992) 396–7